ARTICLE | Article in Press

Radiomics and machine learning analysis to differentiate low grade glioma and encephalitis on non-contrast MRI

Eliseo Picchi · Carlo Di Donna · Armando Ugo Cavallo · Silvia Minosse · Alessandro Castelli · Chiara Giuseppina Bonomi · Francesca Izzi · Alessia Amatruda · Valerio Da Ros · Francesco Garaci · Francesca Di Giuliano

Received: 25 March 2026 / Accepted: 28 September 2026
© The Author(s) 2026

Abstract

Accurate differentiation between low-grade gliomas and encephalitis remains challenging due to overlapping MRI features. This study investigated whether MRI-based radiomics derived from routine non-contrast MRI could improve the differentiation of these entities in diagnostically challenging cases presenting in emergency setting. This retrospective single-center study included 41 patients with ambiguous MRI findings who underwent 3T MRI within 48 h of symptom onset. Radiomic features extracted from T2-FLAIR, DWI, and T1-TSE images, together with laboratory data available at presentation, were analyzed. Random Forest classifiers were developed using selected radiomic features, and model performance was evaluated using nested cross-validation, independent validation, receiver operating characteristic (ROC) analysis, and DeLong's test. The cohort included 23 patients with histologically proven low-grade gliomas and 18 with confirmed encephalitis and was divided into training ($n=31$) and validation ($n=10$) sets. FLAIR-based models showed the best discriminatory performance, achieving an AUC of 0.82 (95% CI: 0.54–1.00) for both the radiomics-only and radiomics-clinical models outperforming T1-weighted (AUC 0.52 for radiomics-only and 0.6 for radiomics-clinical model) and DWI models (AUC 0.72 for both radiomics-only and radiomics-clinical approaches). The combined-sequence radiomics-clinical model achieved an AUC of 0.80 (95% CI: 0.41–1.00), with 100% sensitivity, 80% specificity, and 90% accuracy. Comparison of the ROC curves using DeLong's test did not demonstrate statistically significant differences between the radiomics-only and radiomics-clinical models for any MRI sequence. This proof-of-concept study suggests that radiomic features extracted from routine non-contrast MRI may help differentiate low-grade gliomas from encephalitis in diagnostically challenging cases; however, these preliminary findings warrant validation in larger multicenter cohorts before clinical implementation.

Keywords Radiomics · Machine learning · MRI · Encephalitis · Low-grade glioma

This Article in Press is shared early to give you faster access to new research. It is citable and carries a permanent DOI. The final edited version will replace it automatically.

These authors contributed equally: Eliseo Picchi and Carlo Di Donna.



https://doi.org/10.1038/s41598-026-74097-z

Published online: 10 October 2026

scientific reports

Introduction

Despite major advancements in multiparametric neuroimaging, neuroradiologists still face significant diagnostic challenges in accurately characterizing intracranial lesions particularly when distinguishing between neoplastic and non-neoplastic pathologies[1,2]. This diagnostic challenge is especially true for low-grade gliomas and encephalitis, which often present with overlapping clinical and radiological features, despite having markedly different etiologies, treatment protocols, and prognoses[3–5].

After excluding vascular causes via non-contrast CT, and when lumbar puncture or EEG findings remain inconclusive, MRI becomes the imaging modality of choice, even in emergency settings, to guide diagnosis and prevent unnecessary invasive procedures, such as surgery or biopsies. MRI is the gold standard for evaluating both gliomas and encephalitis. Conventional protocols include T2-weighted, Diffusion-Weighted Imaging (DWI), T2- Fluid Attenuated Inversion Recovery (FLAIR), and 3D T1-weighted sequences, both pre- and post-administration of gadolinium-based contrast agents[6]. However, due to overlapping imaging appearances such as T2/FLAIR hyperintensity, T1 hypointensity, and diffusion restriction, distinguishing these entities may remain challenging even with conventional MRI assessment[7]. The inherent limitations of visual interpretation in extracting subtle intrinsic image features have led to the emergence of radiomics, a rapidly evolving research field focused on the quantitative extraction of image-derived features known as "radiomic features"[8]. These radiomic features, particularly texture-based ones, capture subtle image patterns and voxel relationships that correlate with tissue microstructure, potentially enhancing diagnostic performance and may aid in distinguishing histological subtypes or predicting disease prognosis[9–13].

Given the substantial clinical and radiological overlap between low-grade gliomas and encephalitis, particularly during the early stages of disease, there is a need for objective, non-invasive diagnostic tools to support neuroradiological decision-making.

Previous radiomics and machine-learning studies have demonstrated the potential of quantitative MRI for differentiating gliomas from inflammatory brain lesions. However, many of these investigations relied on multiparametric or contrast-enhanced MRI protocols, focused on broader inflammatory lesion cohorts, or were not specifically designed for the diagnostically challenging subgroup of non-enhancing lesions encountered during the initial emergency work-up.

Therefore, this proof-of-concept study evaluates whether radiomic features extracted exclusively from routinely acquired non-contrast MRI sequences (T2-FLAIR, DWI, and non-contrast T1-weighted images), alone or in combination with presentation-time laboratory data, have the potential to support the differentiation of low-grade gliomas from encephalitis in clinically challenging cases where conventional imaging findings are inconclusive. The goal is to explore the feasibility of this approach rather than to propose a clinically applicable diagnostic tool.

Materials and methods

Patient population

Forty-five brain MRI scans were evaluated in this single-center study, which was conducted in accordance with the Declaration of Helsinki and approved by the Institutional Review Board (N.113.20). Written informed consent was obtained from all patients or their legal representatives prior to the MRI examination. The inclusion criteria were as follows: (1) patients older than 15 years presenting with neurological symptoms; (2) brain MRI performed within 48 h of symptom onset; (3) radiological reports inconclusive between encephalitis and glioma, as identified through PACS retrieval using the keywords "brain inflammation" or "glioma"; (4) diagnosis of encephalitis was established by a multidisciplinary consensus using published and predefined diagnostic criteria

based on the clinical presentation, integrating cerebrospinal fluid (CSF) analysis, microbiological investigations (including CPR when appropriate), neuronal antibody testing for suspected autoimmune encephalitis, and clinical/imaging follow-up[14,15]. A level of diagnostic certainty was assigned to each patient and the final cohort included only cases classified as confirmed encephalitis. The cohort comprised 7 HSV encephalitis 1 VZV encephalitis, 1 HIV-related encephalitis, 1 encephalitis of unknown etiology, 2 anti-LGI1 autoimmune encephalitis, and 3 seronegative autoimmune encephalitis; (5) the diagnosis of low-grade glioma, according to the WHO classification in effect at the time of diagnosis, was confirmed by histopathological examination of brain tissue obtained via biopsy or resection. The molecular status of low-grade glioma was not available for the entire population enrolled in the present study; (6) no prior history of brain surgery, trauma, infection, or treatment before the MRI; and (7) no area of enhancement on T1 weighted images after administration of contrast agent.

To maximize label validity, all encephalitis diagnoses were established independently from the radiomics analysis by a multidisciplinary team using the predefined international diagnostic criteria.

The exclusion criteria were as follows: (1) poor image quality such as significant motion or susceptibility artifacts; (2) radiological signs of ischemic or hemorrhagic stroke (3) incomplete imaging and laboratory data. Cases with persistent diagnostic uncertainty, conflicting clinical and laboratory findings, or insufficient follow-up to establish a final diagnosis were excluded from the study.

Magnetic resonance imaging protocol

All the MRI examinations were performed with a 3T MRI scanner (Ingenia d-Stream, Philips Healthcare, Best, The Netherlands) equipped with 32-channels head coil. The MRI protocol included the following sequences: Diffusion Weighted Image (DWI) with two b-values of 0 and 1000 s/mm^2, T2- and T1-weighted Turbo Spin Echo (TSE) on axial plane, 3D T2-FLAIR, Susceptibility Weighted Imaging (SWI), T1-weighted Turbo Field Echo (TFE) and T1-TSE sequences after the administration of gadobutrol 1.0 mmol/mL with a dose 0.1 mL/kg body weight. Detailed parameters for all imaging sequences are listed in Table 1.

Laboratory data

Both blood test results particularly complete blood count, glucose, blood urea nitrogen (BUN) C-reactive protein (CPR), lactate dehydrogenase (LDH) and cerebrospinal fluid (CSF) findings were evaluated. CSF pleocytosis was defined as a cell count greater than 5 cells per microliter (µL)[16].

All laboratory tests were performed concurrently with MRI acquisition, within 48 h of symptom onset. All laboratory measurements considered as candidate clinical predictors were obtained during the initial emergency evaluation, before establishment of the final diagnosis and before initiation of any disease-specific treatment. Complete laboratory data were available for all included patients; therefore, no missing-data imputation was required.

Table 1 MRI protocol and acquisition parameters.

Parameters	DWI	T2-FLAIR 3D	SWI	T2-TSE	T1-TSE	Post-contrast T1-TFE 3D	Post-contrast T1-TSE
TR/TE (ms)	4500/90	6000/285	22/31	3140/80	2000/20	8/3.5	2000/20
Slice thickness (mm)	3	1	10	3	3	0.9	3
Flip angle (°)	90	90	15	90	90	8	90
Matrix	144 × 142	228 × 228	328 × 328	420 × 350	308 × 226	300 × 300	308 × 226

Abbreviations: DWI, Diffusion Weighted Imaging; FLAIR, FLuid Attenuated Inversion Recovery; SWI, Susceptibility Weighted Imaging; TSE, Turbo Spin Echo; TFE, Turbo Field Echo; TR, Repetition Time; TE, Echo Time.

Volume-of-interest segmentation and feature extraction

All images were anonymized and stored in DICOM format. Using the free open-source software 3D Slicers (version 5.4.0), DWI and T1-TSE images were rigidly co-registered to T2-FLAIR using the module "General registration (BRAINS)", allowing segmentation of the same volume across all sequences. After co-registration, all registrations were visually inspected by an experienced neuroradiologist to ensure anatomical correspondence between T2-FLAIR, DWI, and T1-TSE images before feature extraction. No gross misregistration was observed in the included cases.

Illustrative cases are shown in Figs. 1 and 2.

A three-dimensional volume of interest (VOI) was manually segmented on the hyperintense lesion on T2-FLAIR by an expert neuroradiologist, blinded to the final diagnosis. The same VOI was then propagated to the corresponding DWI and T1-TSE images, ensuring consistency across modalities.

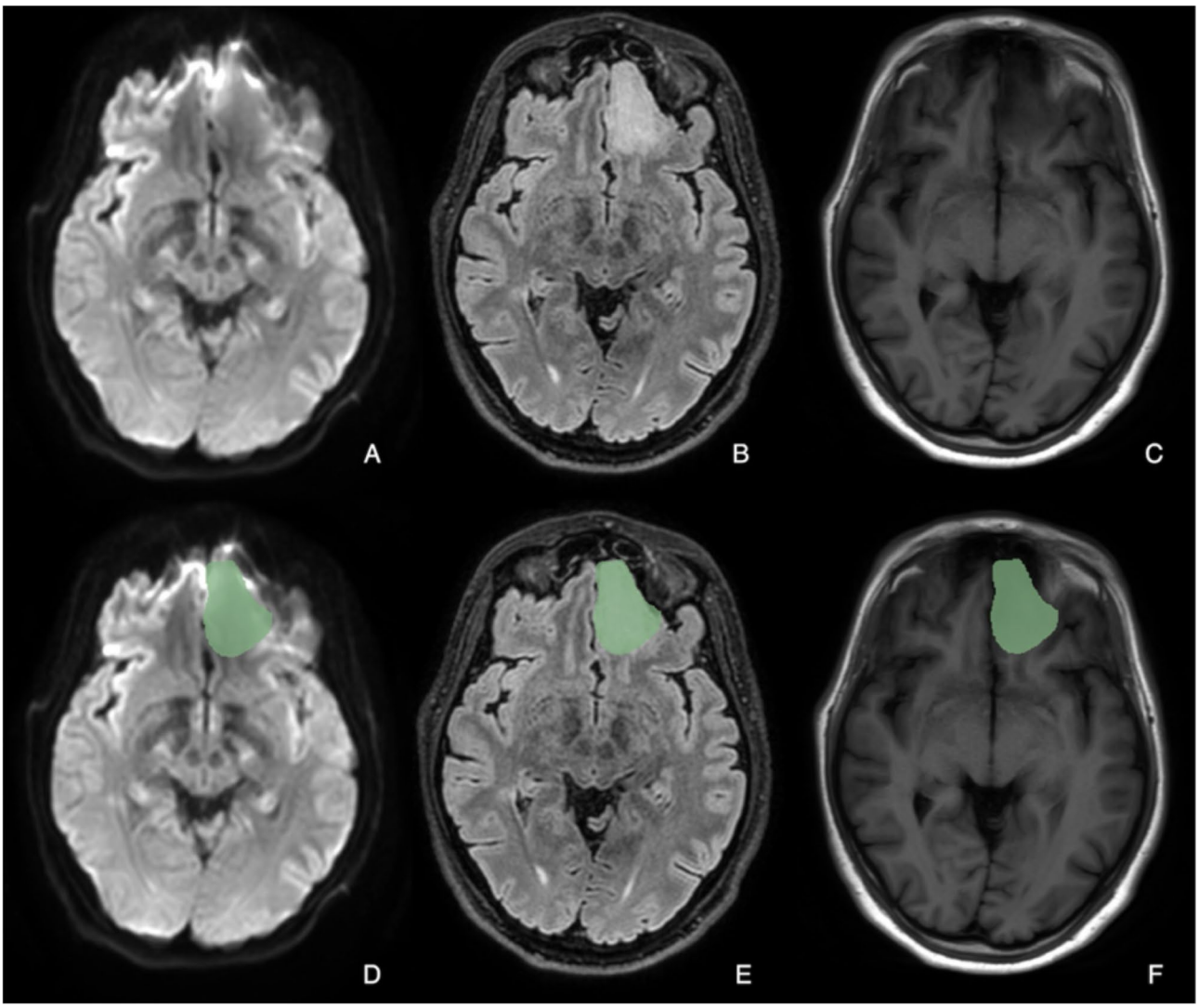


Fig. 1 24-year-old man with histologically confirmed left frontal low-grade glioma. Upper panel: Axial diffusion-weighted imaging (DWI) (**A**), T2 fluid-attenuated inversion recovery (FLAIR) (**B**), and T1 turbo spin echo (TSE) (**C**) weighted images show a well-defined intra-axial lesion in the left frontal cortico-subcortical region. Lower panel: Corresponding lesion segmentation is overlaid on DWI (**D**), T2-FLAIR (**E**), and T1-TSE (**F**) images.

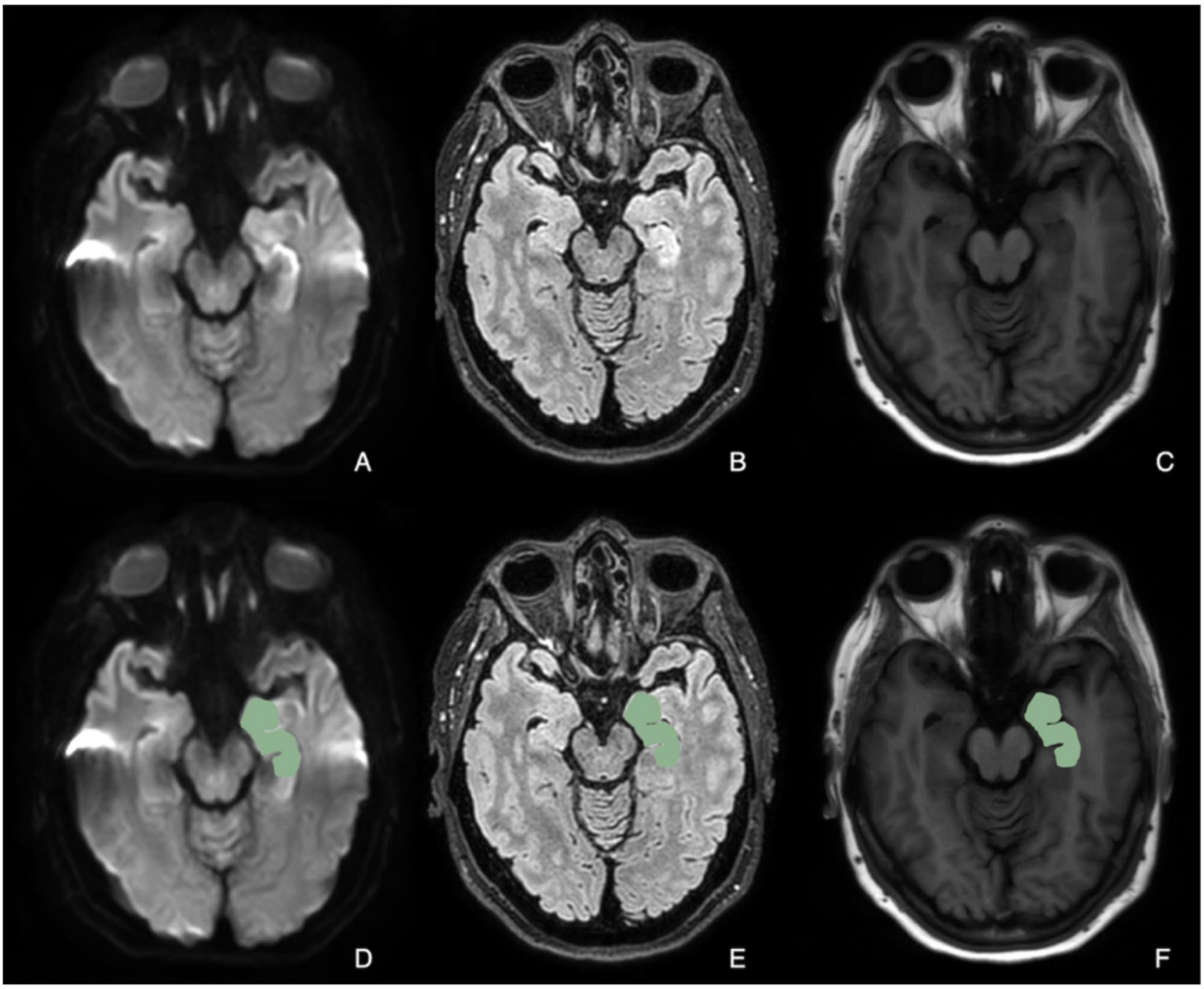


Fig. 2 64-year-old woman with clinically and laboratory-confirmed varicella-zoster virus encephalitis. Upper panel: Axial diffusion-weighted imaging (DWI) (**A**), T2 fluid-attenuated inversion recovery (FLAIR) (**B**), and T1 turbo spin echo (TSE) (**C**) weighted images show a left mesial temporal cortico-subcortical area of restricted diffusion, hyperintense on T2-FLAIR and hypointense on T1-TSE, associated with mild gyral swelling and sulcal effacement. Lower panel: Corresponding lesion segmentation is overlaid on DW (**D**), T2-FLAIR (**E**), and T1-TSE (**F**) images.

From each VOI and for each sequence, a total of 851 radiomic features were extracted using the SlicerRadiomics extension in 3D Slicer, which is based on the PyRadiomics library. The extracted features were classified as follows:

First Order Statistics ($n=18$), Gray Level Co-occurrence Matrix (GLCM, $n=24$), Gray Level Dependence Matrix (GLDM, $n=14$), Gray Level Run Length Matrix (GLRLM, $n=16$), Gray Level Size Zone Matrix (GLSZM, $n=16$), Neighboring Gray Tone Difference Matrix (NGTDM, $n=5$), and 3D shape-based features ($n=14$). All feature classes, except for shape, were extracted both from the original images and from eight wavelet-transformed images. These wavelet components are named according to the application of high-pass (H) or low-pass (L) filters along the three spatial dimensions (X, Y, and Z): HHH, HHL, HLH, HLL, LHH, LHL, LLH, and LLL.

Radiomics preprocessing

Images were analyzed in their native voxel resolution without isotropic resampling or intensity normalization. Gray-level discretization was performed using a fixed bin width of 25. No susceptibility- or eddy current-induced geometric distortion correction was applied to the DWI images prior to image registration.

Feature definitions followed the Image Biomarker Standardisation Initiative (IBSI) recommendations implemented in PyRadiomics.

Feature preprocessing and selection

To ensure a robust pipeline, a rigorous validation framework was adopted. The radiomics workflow followed a strict order of operations: splitting, scaling, feature selection, model training/tuning, final evaluation.

The dataset was divided into a training set and an independent test set (with a 75:25 ratio) using the createDataPartition function from the R caret package, with stratification according to diagnostic class. A random seed was specified before partitioning (set.seed(0.01)) to ensure reproducibility.

Feature preprocessing and selection were performed exclusively on training data within each resampling iteration to avoid information leakage.

First, radiomic features were standardized using z-score normalization (mean centering and scaling to unit variance). The scaling parameters were estimated from the training partition and subsequently applied to the corresponding validation data.

To reduce redundancy and dimensionality, a two-step feature reduction procedure was implemented. Features with near-zero variance were removed, followed by elimination of highly correlated variables using a Pearson correlation threshold of 0.90.

Subsequently, supervised feature selection was performed using regularized logistic regression implemented through elastic-net regularization. A grid search explored alpha values of 0.5 and 1.0, corresponding to elastic-net and LASSO penalties, respectively, while lambda values were optimized through internal cross-validation. Features with non-zero regression coefficients were retained and used for subsequent model training.

For radiomics-clinical models, clinical variables were not subjected to feature selection and were incorporated as fixed predictors after radiomic feature selection.

Radiomics data analysis

Separate analyses were performed for T1-weighted, FLAIR, DWI, and combined multi-sequence radiomic datasets.

Classification models were developed using Random Forest (RF) classifiers. Two model configurations were evaluated:

1) a radiomics-only model using selected radiomic features;
2) a combined radiomics-clinical model obtained by concatenating the selected radiomic features with clinical variables.

The clinical variables included in the machine-learning models were red blood cell count, hemoglobin, hematocrit, platelet count, white blood cell count, blood glucose, blood urea nitrogen, C-reactive protein (CRP), and lactate dehydrogenase (LDH) available at presentation. Although cerebrospinal fluid (CSF) findings were collected for diagnostic characterization, CSF positivity/negativity and other diagnostic CSF results were not included as model predictors to avoid potential label leakage. The clinical variables were prespecified a priori based on their routine availability during the initial emergency assessment and their potential relevance in the differential diagnosis between inflammatory and neoplastic brain lesions. No data-driven selection of clinical variables was performed.

To obtain an unbiased estimate of model performance and account for feature selection during model development, a nested cross-validation strategy was employed on the training set.

The outer loop consisted of a stratified 10-fold cross-validation used for performance estimation. Within each outer training partition, feature preprocessing, correlation filtering, elastic-net/LASSO feature selection, and RF hyperparameter optimization were repeated independently.

The inner loop consisted of a stratified 5-fold cross-validation used to optimize elastic-net/LASSO regularization parameters and RF hyperparameters.

For the RF classifier, the optimal number of variables randomly sampled at each split (mtry) was determined through cross-validation.

Following nested cross-validation, the final model was retrained using the entire training set. Feature preprocessing, filtering, and elastic-net/LASSO feature selection were repeated on the full training dataset, and the resulting feature subset was used to train the final RF classifier subsequently evaluated on the independent test set.

All preprocessing operations, including scaling and correlation filtering, were fitted exclusively within each training fold and subsequently applied to the corresponding validation fold. The independent test set was not used for preprocessing, feature selection, or hyperparameter tuning and remained untouched until final model evaluation. The classification threshold was determined post hoc from the ROC curve generated on the independent test set by maximizing Youden's index.

Model evaluation

Model discrimination was assessed using the area under the receiver operating characteristic curve (AUC). For nested cross-validation, out-of-fold predictions generated by the outer loop were aggregated to calculate AUC values and corresponding 95% confidence intervals.

The final models were evaluated on an independent test set. Receiver operating characteristic (ROC) curves were generated, and AUC values with 95% confidence intervals were calculated using the DeLong method. Optimal classification thresholds were identified according to the Youden index. Accuracy, sensitivity, specificity, positive predictive value (PPV), and negative predictive value (NPV) were calculated together with exact binomial 95% confidence intervals.

Comparisons between ROC curves were performed using the DeLong test.

Model calibration was evaluated through calibration plots and the Brier score. Given the limited size of the independent test cohort, calibration analyses were considered exploratory.

Clinical utility was assessed using Decision Curve Analysis (DCA) as exploratory, comparing the net benefit of the radiomics-only and radiomics-clinical models across a range of threshold probabilities.

Statistical analysis

The statistical analysis was performed with the software R version 3.4.4[17]. Categorical variables were expressed as absolute numbers and percentages, while continuous variables were expressed as mean ± standard deviation (SD).

The T test and the Wilcoxon test were used to compare continuous variables when appropriate.

All steps described above are summarized in the workflow shown in Fig. 3.

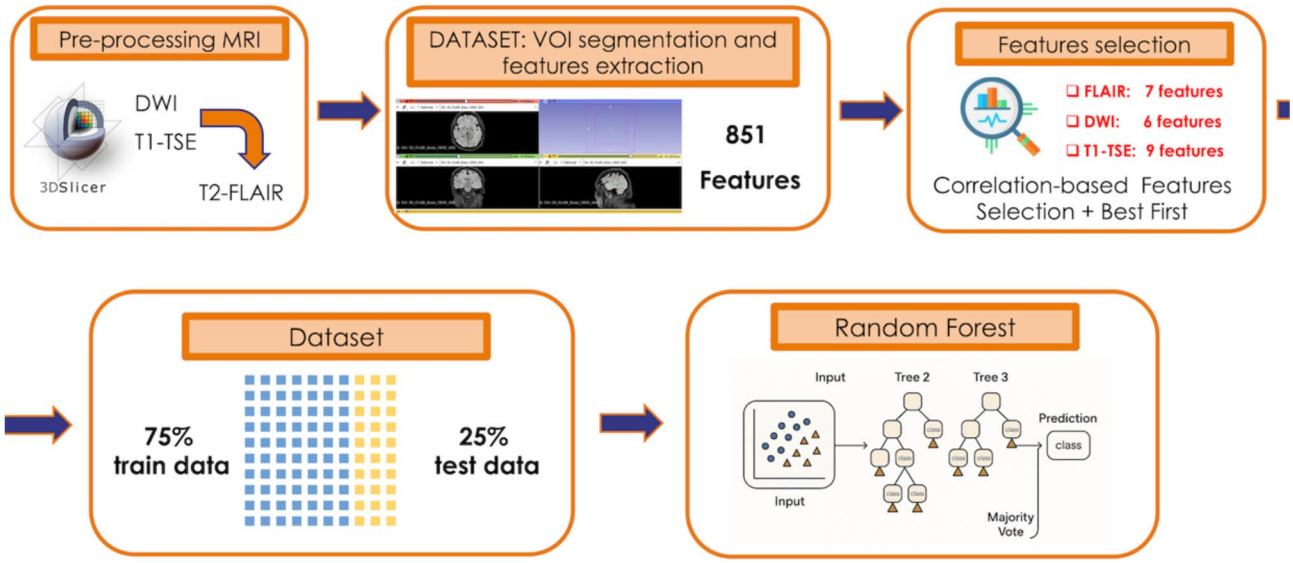


Fig. 3 Workflow summarizing all steps of the analysis pipeline.

Table 2 Summary of demographic, clinical and biochemical characteristics analysis.

Entire dataset	Glioma patients (*n*.23)	Encephalitis patients (*n*.18)	*p*-value
Gender (M/F, % male)	14/9 (60.8%)	7/11 (38.9%)	0.1713
Age (years old) [range in year]	58.87 ± 13.70	60.17 ± 17.63	0.6278
Red Blood Cells (million/μL)	4.65 ± 0.70	4.60 ± 0.61	0.8131
Hemoglobin (g/dL)	13.62 ± 1.91	13.57 ± 2.22	0.9404
Hematocrit (%)	40.84 ± 5.10	40.10 ± 6.53	0.6954
Platelets (thousand/μL)	229.48 ± 57.23	247.83 ± 85.98	0.4416
White Blood Cells (thousand/μL)	9.79 ± 4.44	8.81 ± 2.81	0.3973
Glucose (mg/dL)	102.87 ± 37.95	129.56 ± 56.91	0.0976
BUN (mg/dL)	34.96 ± 18.23	36.94 ± 16.78	0.7191
CRP (mg/L)	9.26 ± 38.94	7.46 ± 15.13	0.8399
LDH (U/L)	128.30 ± 92.12	166.28 ± 68.51	0.1383
CSF	23 Negative	18 Positive	

Abbreviations: M, male; F, female; BUN, blood urea nitrogen; CRP, C-reactive protein; LDH, Lactate Dehydrogenase; CSF, Cerebro-Spinal Fluid. Data are express as mean and standard deviation.

Results

A total of 45 patients were extracted from the local PACS by using the keywords "inflammation" or "glioma". Patients with non-diagnostic or lower quality of MR images and/or lack of CSF blood chemistry tests were excluded. The final evaluated population was made up by 41 patients of which 23 patients with histologically proven low-grade glioma and 18 patients with signs, symptoms and biochemical findings of CNS inflammation. Of these, 31 patients were assigned to the training data set (glioma, $n = 17$; encephalitis, $n = 14$), and 10 patients were assigned to the validation data set (glioma, $n = 6$; encephalitis, $n = 4$). Clinical and biochemical data are summarized in Tables 2 and 3.

All patients, at visual evaluation, exhibited slightly increased signal intensity on diffusion-weighted imaging (DWI, b-value=1000s/mm^2), along with hyperintense areas on T2-FLAIR images.

For each MRI sequence, a total of 851 radiomic features were initially extracted.

Table 3 Findings from the analysis of basic demographic and clinical data within the training and validation data sets.

	Training data set ($n=31$)			Validation data set ($n=10$)		
	Glioma patients	Encephalitis patients	*p*-value	Glioma patients	Encephalitis patients	*p*-value
Number of patients	17	14		6	4	
Gender (M/F, % male)	48.39%	51,61	0.39	50%	50%	0.24
Age (years old) [range in year]	58.29 ± 12.82	56.50 ± 18.89	0.77	48.83 ± 14.41	65.00 ± 18.74	0.2
Red Blood Cells (million/µL)	4.61 ± 0,75	4.69 ± 0.65	0.76	4.77 ± 0.70	4.30 ± 0.26	0.15
Hemoglobin (g/dL)	13.46 ± 2.16	13.93 ± 2.22	0.56	13.74 ± 1.94	13.15 ± 1.46	0.18
Hematocrit (%)	40.46 ± 5.79	41.41 ± 6.24	0.66	41.02 ± 5.52	38.98 ± 4.18	0.12
Platelets (thousand/µL)	226.00 ± 61.72	254.50 ± 92.71	0.34	247.80 ± 45.60	232.00 ± 52.30	0.69
White Blood Cells (thousand/µL)	10.17 ± 4.98	8.99 ± 3.14	0.43	8.39 ± 2.05	8.53 ± 2.25	0.66
Glucose (mg/dL)	103.18 ± 42.17	130.64 ± 60.10	0.16	101.80 ± 16.02	101.75 ± 32.00	0.44
BUN (mg/dL)	35.53 ± 21.18	40.00 ± 17.66	0.53	32.00 ± 6.20	29.75 ± 7.93	0.14
CRP (mg/L)	12.29 ± 45.25	6.94 ± 16.73	0.66	5.10 ± 8.52	3.9 ± 5.80	0.15
LDH (U/L)	126.18 ± 100.95	164.18 ± 76.52	0.24	170.00 ± 29.77	122.25 ± 84.94	0.28
CSF	17 Negative	14 Positive		6 Negative	4 Positive	

Abbreviations: M, male; F, female; BUN, blood urea nitrogen; CRP, C-reactive protein; LDH, Lactate Dehydrogenase; CSF, Cerebro-Spinal Fluid. Data are express as mean and standard deviation.

Table 4 Performance of radiomic models in nested cross validation.

MRI sequence	Radiomics model AUC (95% CI)	Radiomics + clinical model AUC (95% CI)
T1	0.67 (0.46–0.87)	0.65 (0.44–0.85)
FLAIR	0.62 (0.41–0.82)	0.58 (0.38–0.79)
DWI	0.54 (0.33–0.76)	0.51 (0.3–0.73)
Multi-sequence	0.7 (0.51–0.9)	0.66 (0.46–0.86)

Abbreviations: DWI, Diffusion Weighted Imaging; FLAIR, FLuid Attenuated Inversion Recovery.

Nested cross validation performance

The performance of the radiomics-only and radiomics-clinical models was first assessed using a nested cross-validation framework on the training cohort. Overall, the inclusion of clinical variables improved the discriminatory performance of most MRI sequence-based models. The highest performance was observed for T1 weighted sequence, whereas the combined-sequence model showed slightly higher performance compared with the best single-sequence model.

The AUC values obtained by nested cross-validation, together with their 95% confidence intervals, are summarized in Table 4. The selection frequency of individual radiomic features across the outer cross-validation folds is reported in Supplementary Table 1.

Independent test set performance

Feature selection identified 23 relevant radiomic features from T2-FLAIR, 20 from T1-TSE, 81 from DWI and 16 for all sequences combined (Supplementary materials Table 2).

On the independent test cohort the diagnostic performance varied substantially across MRI sequences.

The T1-weighted models showed poor discriminative ability, with AUC values of 0.52 (95% CI: 0.07–0.97) for the radiomics-only model and 0.60 (95% CI: 0.19–1.00) after the addition of clinical variables. In contrast, FLAIR-based models demonstrated good discriminatory performance, achieving an AUC of 0.82 (95% CI: 0.54–1.00) for both the radiomics-only and radiomics-clinical approaches. Similarly, DWI-based models yielded moderate-to-good performance, with an AUC of 0.72 (95% CI: 0.32–1.00), which was not further improved by the incorporation of clinical variables. Good performance, but lower than FLAIR-based models, was observed

for the combined-sequence model integrating radiomic and clinical information, which achieved an AUC of 0.80 (95% CI: 0.41–1.00), with a sensitivity of 100%, specificity of 80%, and overall accuracy of 90%.

Although the addition of clinical variables resulted in numerically higher performance for some models, comparison of the ROC curves using DeLong's test did not demonstrate statistically significant differences between the radiomics-only and radiomics-clinical models for any MRI sequence (all $p > 0.05$).

Detailed performance metrics obtained on the independent test set are summarized in Table 5. Model-specific hyperparameters, classification thresholds selected using Youden's index, and corresponding confusion matrices are reported in Supplementary Table 3 and Fig. 4.

Calibration curves

Calibration analysis showed variable performance across MRI sequences. The T1-based models exhibited the highest Brier scores, indicating relatively poor agreement between predicted probabilities and observed outcomes (radiomics: 0.313; radiomics-clinical: 0.324). In contrast, the FLAIR-based models demonstrated the lowest Brier scores (radiomics: 0.210; radiomics-clinical: 0.221), suggesting better calibration performance. Intermediate results were observed for the DWI-based models (radiomics: 0.230; radiomics-clinical: 0.241) and for the multi-sequence models (radiomics: 0.211; radiomics-clinical: 0.226). Overall, the addition of clinical variables did not result in a substantial improvement in calibration performance. Beyond discrimination, reliable probability calibration is essential for supporting threshold-based clinical decisions, as emphasized by recent MRI radiomics research[18]. However, robust calibration assessment requires larger validation cohorts; therefore, given the limited size of the independent test cohort, these findings should be interpreted with caution.

Results are summarized in Fig. 5; Table 6.

Decision curve analysis

Decision curve analysis (DCA) was performed as an exploratory assessment of net benefit for most of the evaluated models (Fig. 6). For the T1-TSE-, FLAIR-, and DWI-based models, both the radiomics-only and radiomics-clinical approaches yielded a higher net benefit than the "treat-all" strategy across a range of threshold probabilities.

Table 5 Diagnostic performance of radiomics-only and radiomics-clinical models on the independent test set.

MRI sequence	Model	AUC (95% CI)	Accuracy (95% CI)	Sensitivity (95% CI)	Specificity (95% CI)	PPV (95% CI)	NPV (95% CI)	DeLong *p*
T1	Radiomics	0.52 (0.07–0.97)	0.30 (0.07–0.65)	0.40 (0.05–0.85)	0.20 (0.01–0.72)	0.33 (0,04–0,78)	0.25 (0.01–0.81)	0.40
T1	Radiomics + clinical	0.60 (0.19–1.00)	0.30 (0.07–0.65)	0.40 (0.05–0.85)	0.20 (0.01–0.72)	0.33 (0.04–0.78)	0.25 (0.01–0.81)	—
FLAIR	Radiomics	0.82 (0.54–1.00)	0.80 (0.44–0.97)	0.60 (0.15–0.95)	1.00 (0.48–1.00)	1.00 (0.29–1.00)	0.71 (0.29–0.96)	1.00
FLAIR	Radiomics + clinical	0.82 (0.50–1.00)	0.80 (0.44–0.97)	0.60 (0.15–0.95)	1.00 (0.48–1.00)	1.00 (0.29–1.00)	0.71 (0.29–0.96)	—
DWI	Radiomics	0.72 (0.32–1.00)	0.80 (0.44–0.97)	0.80 (0.28–0.99)	0.80 (0.28–0.99)	0.80 (0.28–0.99)	0.80 (0.28–0.99)	1.00
DWI	Radiomics + clinical	0.72 (0.32–1.00)	0.80 (0.44–0.97)	0.80 (0.28–0.99)	0.80 (0.28–0.99)	0.80 (0.28–0.99)	0.80 (0.28–0.99)	—
Multi-sequence	Radiomics	0.72 (0.37–1.00)	0.80 (0.44–0.97)	0.80 (0.28–0.99)	0.80 (0.28–0.99)	0.80 (0.28–0.99)	0.80 (0.28–0.99)	0.70
Multi-sequence	Radiomics + clinical	0.80 (0.41–1.00)	0.90 (0.55–1.00)	1.00 (0.48–1.00)	0.80 (0.28–0.99)	0.83 (0.36–1.00)	1.00 (0.40–1.00)	—

Performance metrics were calculated on the independent test set using the optimal cutoff determined by the Youden index. Values are reported with exact 95% confidence intervals. DeLong's test was used to compare the ROC curves of radiomics-only and radiomics-clinicalmodels.

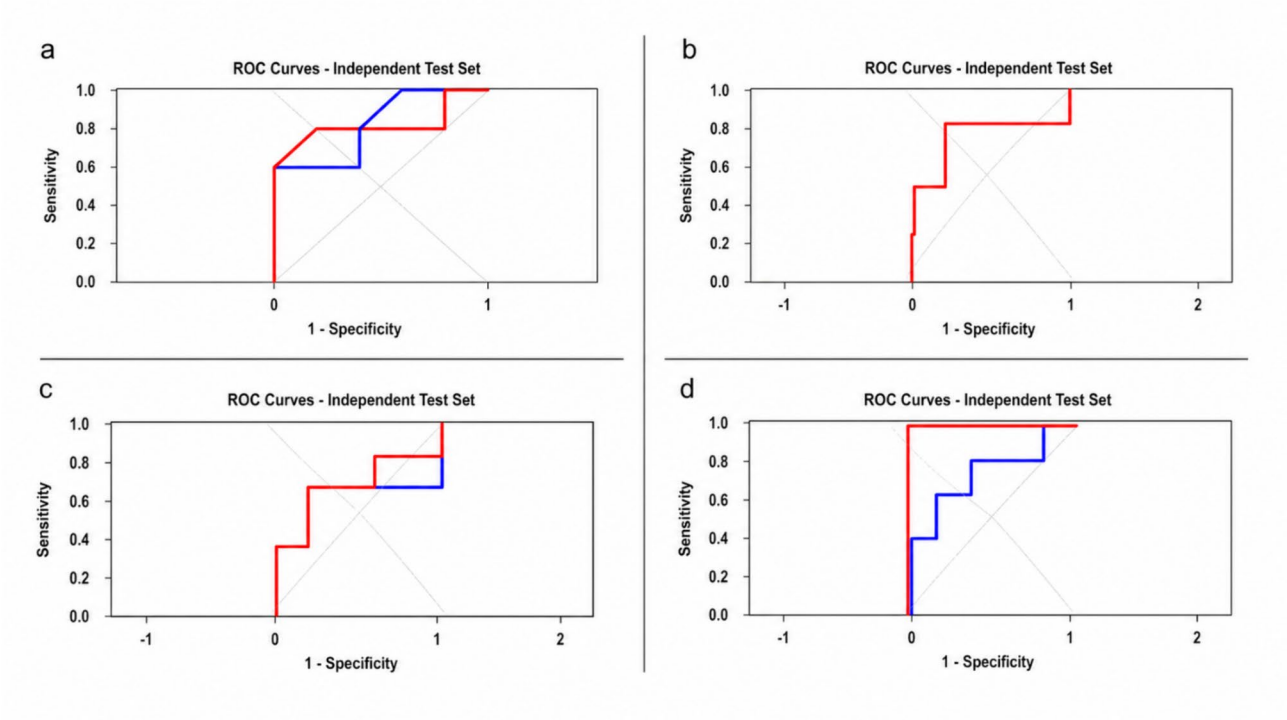


Fig. 4 Receiver operating characteristic (ROC) curves comparing the performance of the radiomics-only model (blue curve) and the combined radiomics plus clinical data model (red curve). Panels represent models built using different MRI sequences: (**a**) T2-FLAIR, (**b**) DWI, (**c**) T1-weighted imaging, and (**d**) the combination of all MRI sequences.

However, the T1-based models showed a more limited area of clinical utility compared with the FLAIR and DWI models.

For the multi-sequence models, the radiomics-only approach maintained a favorable net benefit across a broad range of threshold probabilities. In contrast, the radiomics-clinical model showed a marked decrease in net benefit at threshold probabilities around 50%, with the decision curve falling below the "treat-none" strategy at higher thresholds.

Given the test-set size of only 10 patients, these estimates should be confirmed in larger, externally validated cohorts to be interpreted as evidence of clinical utility or implementation readiness.

Discussion

This study aimed to assess the feasibility of a radiomics-based random forest model for differentiating gliomas from encephalitis using quantitative features extracted from non-contrast-enhanced T2-FLAIR, T1-weighted, and DWI brain MRI sequences.

Our findings suggest that quantitative radiomic analysis may capture subtle imaging differences between these two entities even in the absence of contrast agent administration in neurologically compromised or uncooperative patients and in diagnostically challenging cases with overlapping clinical and laboratory features. Given the limited sample size, these observations should be interpreted as preliminary proof-of-concept evidence rather than definitive evidence of diagnostic performance. Baseline demographic and laboratory characteristics did not differ significantly between glioma and encephalitis patients in either the training or validation cohorts, supporting the notion that the observed classification performance was primarily driven by imaging-derived features rather than confounding clinical variables. These findings suggest that radiomics may represent a complementary

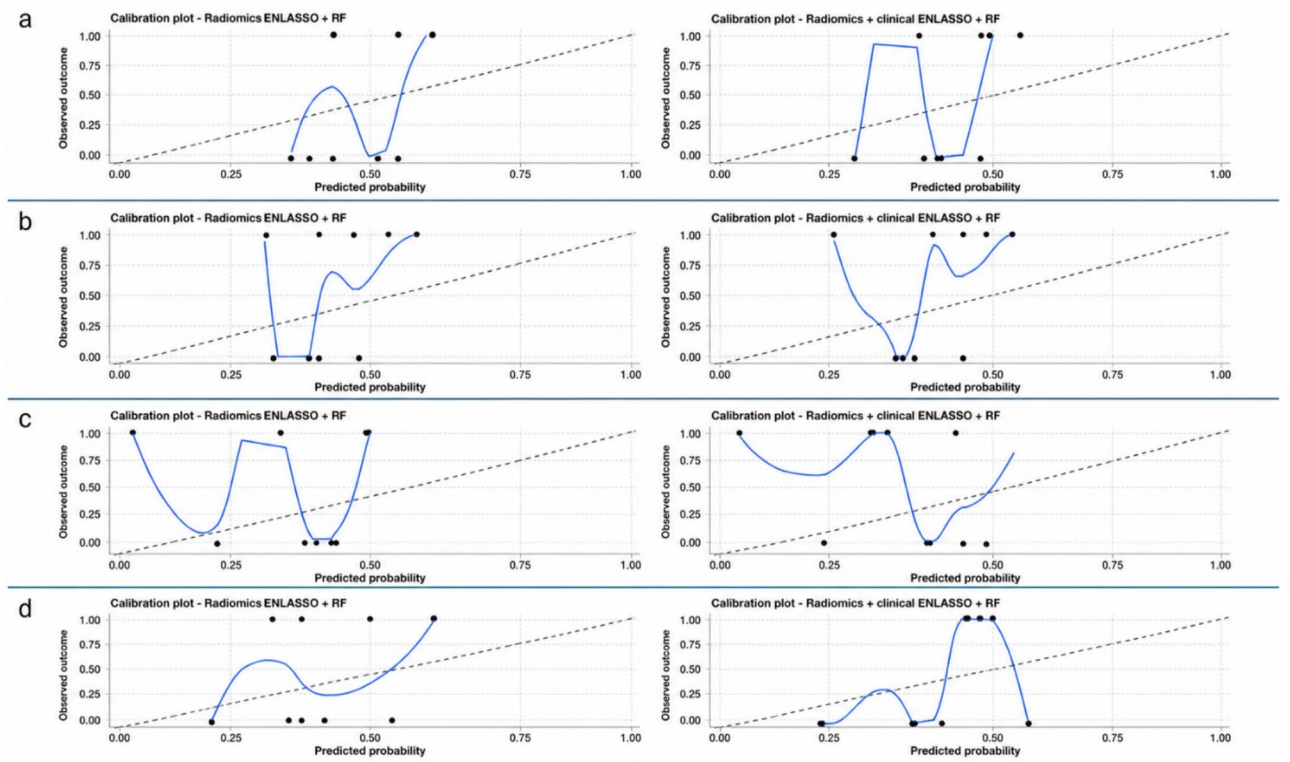


Fig. 5 Calibration curves of the predictive models. The left panels show the calibration curves for the radiomics-only models, while the right panels show the calibration curves for the combined radiomics plus clinical data models. Panels correspond to models developed using different MRI sequences: (**a**) T2-FLAIR, (**b**) DWI, (**c**) T1-weighted imaging, and (**d**) the combination of all MRI sequences.

Table 6 Calibration performance of radiomics-only and radiomics-clinical models on the independent test set.

MRI sequence	Radiomics model Brier score	Radiomics + clinical model Brier score
T1	0.313	0.324
FLAIR	0.210	0.221
DWI	0.230	0.241
Multi-sequence	0.211	0.226

Lower Brier scores indicate better agreement between predicted probabilities and observed outcomes.

quantitative imaging biomarker worthy of further investigation, particularly in diagnostically challenging cases. Feature extraction and selection identified a set of discriminative radiomic parameters predominantly including first-order statistics, shape features, and texture-based descriptors. These features may reflect underlying pathological heterogeneity and microstructural complexity, supporting their relevance as non-contrast imaging biomarkers for lesion characterization. Notably, the integration of radiomic features with complementary laboratory data resulted in numerically higher performance metrics for several models and may pave the way for promising results for differentiating low-grade glioma and encephalitis. However, these differences were not statistically significant according to the DeLong test and should therefore be interpreted cautiously. The highest diagnostic accuracy was achieved using T2-FLAIR and DWI sequences, although T1-weighted images also demonstrated good performance when combined with laboratory data.

The selected radiomic features mainly belonged to shape, first-order, and texture feature families, including GLCM, GLDM, and GLSZM descriptors. Among these, several first-order features extracted from wavelet-transformed images, such as mean absolute deviation and kurtosis, were more frequently retained by models

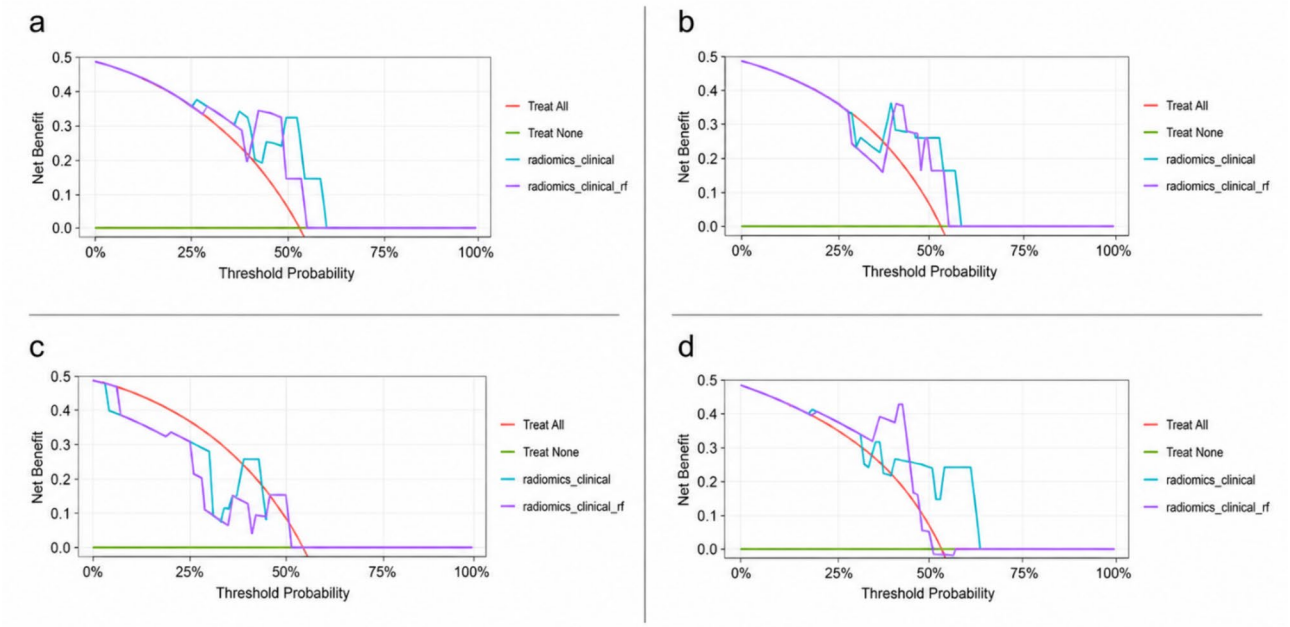


Fig. 6 Decision curve analysis (DCA) of the predictive models. Panels correspond to models developed using different MRI sequences: (**a**) T2-FLAIR, (**b**) DWI, (**c**) T1-weighted imaging, and (**d**) the combination of all MRI sequences. The decision curves illustrate the net clinical benefit of each model across a range of threshold probabilities.

identifying low-grade glioma. However, the biological interpretation of individual radiomic features should be approached with caution. Given the relatively limited sample size of the present study, the feature selection process is likely to be unstable, and different but highly correlated radiomic features may be selected across different training subsets. Therefore, no specific histopathological meaning can be attributed to the selected features without validation against tissue-based reference standards. Rather than focusing on single radiomic descriptors, it is more appropriate to consider the broader feature families represented in the final models. Texture-based radiomic features may provide indirect information about the underlying tissue microenvironment. In particular, GLSZM features quantify the size and distribution of homogeneous gray-level zones within a lesion, whereas GLDM features describe gray-level dependencies within a defined neighborhood. These feature families may capture differences in image heterogeneity and spatial organization at the MRI level. However, because the present study did not include tissue-level validation, it cannot be concluded that these imaging-derived features directly reflect specific histopathological mechanisms. These biological interpretations remain speculative and should be regarded only as plausible hypotheses to explain the discriminatory ability of these feature families. No direct correspondence between the selected radiomic features and specific histopathological mechanisms can be inferred without validation against tissue-level reference standards.

The frequent retention of wavelet-derived features further suggests that multiscale texture analysis captures complementary imaging information that is not readily appreciable on conventional visual assessment. Similarly, radiomic features extracted from T2-FLAIR, T1-weighted, and DWI sequences may reflect different aspects of lesion heterogeneity, tissue organization, and diffusion characteristics, thereby providing complementary information for model discrimination. Nevertheless, because feature selection may vary across datasets, these observations should be interpreted as evidence that multiscale texture information is diagnostically valuable rather than proof of the biological significance of any individual radiomic feature.

In our analysis the highest accuracy and specificity have been reached from machine learning analysis of T2-FLAIR, even though DWI has shown optimal sensitivity; these findings are broadly consistent with those reported in earlier studies. Accordingly, texture features extracted from T2-weighted images appear to

provide more informative representations of lesion-related pathophysiological changes than those derived from T1-weighted images[7,19]. A noteworthy finding of this study is the prominent selection of wavelet-based features, which underscores the value of multiscale analysis. These wavelet-based features capture hidden and subtle patterns not visible to the human eye in the original images, making them particularly promising for highlighting multi-resolution heterogeneity. Together, these results suggest that incorporating multiscale analysis should be considered in future radiomics pipelines to fully exploit this information.

These data suggest the utility of radiomics applied to non-contrast brain MRI for differentiating low-grade glioma from encephalitis, showing promising predictive performance in line with a previous study[1]. Although different authors have selected various MRI sequences for radiomic and machine learning analyses of gliomas[20–28], the present study focused on non-contrast basic sequences, particularly those routinely acquired in emergency MRI settings, such as T1-weighted, T2-FLAIR, and DWI sequences. Similarly, previous studies have explored radiomic analyses using different MRI sequences. For glioma grading, contrast-enhanced T1-weighted imaging has been widely used and has shown strong discriminative performance, either alone or in combination with T2-FLAIR sequences[29,30]; moreover, Tian et al. and Ge et al. reported that radiomic features extracted from contrast-enhanced T1-weighted images achieved superior performance compared with other single MR sequences for glioma grading[11,31], whereas Liang et al. showed that T2-weighted imaging provided the highest predictive accuracy for glioma IDH genotype, with lower performance observed for contrast-enhanced T1-weighted imaging[32,33].

Interestingly, the model combining radiomic features from all MRI sequences, even combined with clincal data, did not outperform the single-sequence T2-FLAIR model. A possible explanation is that the integration of features from multiple sequences substantially increased the dimensionality of the feature space relative to the available sample size, potentially introducing redundant or noisy information and reducing model generalizability. In addition, the relatively small sample size may have limited the stability of model training and hyperparameter tuning, increasing the risk of overfitting and reducing the ability to fully exploit the additional information provided by the multimodal feature set.

Despite these encouraging findings, the wide confidence intervals observed across all models reflect the substantial statistical uncertainty associated with the very small independent test cohort. The discrepancy between the modest nested cross-validation performance and the higher AUCs observed for some models in the independent test set was limited but may partly reflect sampling variability and instability of performance estimates. The test-set results should therefore be interpreted cautiously in light of the small sample size, the wide confidence intervals, and the other methodological limitations of this proof-of-concept study; confirmation in larger independent cohorts is warranted.

An important strength of this study is the exclusive use of routinely acquired non-contrast MRI sequences, which may increase its clinical relevance in emergency diagnostic settings where contrast administration is not feasible or may be delayed. In routine clinical practice, differentiating gliomas from encephalitis can be challenging, particularly in atypical presentations or early disease stages. A fast emergency MRI protocol based on T1-weighted, DWI, and T2-FLAIR sequences could provide a suitable framework for future radiomics-based decision-support strategies aimed at facilitating diagnostic assessment in emergency settings. Whether such approaches improve patient management, reduce unnecessary interventions, or decrease healthcare costs remains to be demonstrated in prospective studies. Radiomics-based models derived from standard MRI sequences may represent promising decision-support tools. However, their clinical utility should be confirmed in larger prospective multicenter studies with external validation before routine implementation can be considered.

Several previous studies have reported promising results using radiomics or machine-learning approaches to differentiate gliomas from inflammatory brain lesions. Rather than introducing a novel classification task, the present study addresses a more specific clinical scenario. Our cohort was intentionally restricted to patients with clinically ambiguous, non-enhancing lesions examined within 48 h of symptom onset, reflecting a common real-world setting in which conventional MRI interpretation is particularly challenging. Furthermore, the proposed workflow relies exclusively on routinely acquired non-contrast MRI sequences (T2-FLAIR, DWI, and

T1-weighted imaging) combined with laboratory parameters available at presentation, thereby reflecting imaging protocols commonly used in emergency clinical practice. Accordingly, the main contribution of this proof-of-concept study lies in evaluating the feasibility of a simplified radiomics workflow within this specific diagnostic context rather than proposing a novel diagnostic application or a clinically ready decision-support tool. Although several combined models achieved numerically higher performance than radiomics-only models, these differences did not reach statistical significance. Finally, the workflow is based on a relatively simple and interpretable machine-learning framework using standard radiomic features and Random Forest classification, facilitating methodological transparency and reproducibility.

Given the exploratory nature of this study, several limitations should be acknowledged. An important limitation is the small sample size relative to the high-dimensional radiomic feature space, particularly the limited independent validation cohort, which may have resulted in model-selection instability, optimistic performance estimates, and unstable estimates of diagnostic performance despite stratified data partitioning, nested cross-validation, and maintenance of a separate test set throughout the analysis. Another limitation is the use of a biologically heterogeneous encephalitis cohort, including both infectious and autoimmune subtypes. Although this design reflects the real-world clinical differential diagnosis encountered before etiological confirmation, different pathogenic mechanisms may produce distinct imaging phenotypes and radiomic signatures. Consequently, the proposed classifier should be interpreted as distinguishing low-grade glioma from a heterogeneous spectrum of encephalitis rather than from any specific encephalitis subtype, and its performance should be validated in larger subtype-specific cohorts.

Furthermore, no external validation cohort was available, due to the monocentric nature of the study. Another limitation of the present study is the lack of an assessment of radiomic feature reproducibility. Inter-reader and intra-reader variability, as well as feature robustness to segmentation variability, were not evaluated and should be investigated in future studies. The absence of isotropic resampling, intensity normalization, and dedicated DWI distortion correction may have affected radiomic feature stability across sequences with different spatial resolutions and contrasts.

Therefore, the present findings should be considered preliminary and hypothesis-generating, and future multicenter studies with larger independent datasets are needed before translation into routine clinical decision-making. Moreover, our encephalitis cohort included multiple infectious and autoimmune encephalitis subtypes, biological heterogeneity may have influenced imaging phenotypes and the resulting radiomic signatures: while this reflects real-world clinical practice in the differential diagnosis of gliomas and encephalitis, it may limit the model's generalizability to individual encephalitis subtypes.

In conclusion, this study provides preliminary proof-of-concept evidence that radiomic features extracted from routine non-contrast-enhanced T2-FLAIR, T1-weighted, and DWI sequences may contribute to the characterization of imaging phenotypes associated with low-grade gliomas and encephalitis. Notably, T2-FLAIR alone achieved diagnostic performance comparable to that obtained using radiomic features extracted from all MRI sequences, suggesting that this sequence may represent the most informative non-contrast MRI sequence for radiomic characterization in this clinical setting.

The integration of radiomic features with laboratory data yielded numerically higher performance metrics in several analyses. However, the absence of statistically significant differences according to the DeLong test indicates that the potential incremental value of laboratory variables should be confirmed in larger independent cohorts before any clinical translation.

Supplementary Information The online version contains supplementary material available at https://doi.org/10.1038/s41598-026-74097-z.

Author contributions Conceptualization: E.P. and F.D.G.Methodology: E.P.; C.D.D.; S.M. Formal analysis and investigation: C.D.D.; A.U.C.; S.M.Resources: A.C.; C.G.B.; A.A.; V.D.R.Writing - original draft preparation and revised manuscript: E.P.; C.D.D.; A.U.C; S.M.Supervision: F.I.; F.G.; F.D.G.

Funding This research is co-funded by the Ministry of University and Research within the Complementary National Plan PNL-I.1 "Research initiatives for innovative technologies and pathways in the health and welfare sector"-"DARE - Digital Lifelong Prevention" (project code: PNC0000002 - CUP: B53C22006450001).

Data availability The data that support the findings of this study are not openly available due to reasons of sensitivity and are available from the corresponding author upon reasonable request. Data are located in controlled access data storage at University Hospital of Rome Tor Vergata.

Declarations

Competing interests The authors declare no competing interests.

Human ethics and consent to participate declarations This retrospective study was approved by the Institutional Review Board (N.113.20) and conducted in accordance with the Declaration of Helsinki and its subsequent amendments. Written informed consent was obtained from all patients or their legal representatives prior to the MRI examination.

Open Access This article is licensed under a Creative Commons Attribution 4.0 International License, which permits use, sharing, adaptation, distribution and reproduction in any medium or format, as long as you give appropriate credit to the original author(s) and the source, provide a link to the Creative Commons licence, and indicate if changes were made. The images or other third party material in this article are included in the article's Creative Commons licence, unless indicated otherwise in a credit line to the material. If material is not included in the article's Creative Commons licence and your intended use is not permitted by statutory regulation or exceeds the permitted use, you will need to obtain permission directly from the copyright holder. To view a copy of this licence, visit http://creativecommons.org/licenses/by/4.0/.

References

1. Wu, W. et al. Differentiation of glioma mimicking encephalitis and encephalitis using multiparametric MR-based deep learning. *Front. Oncol.***11**, 639062 (2021).
2. Piper, K., Foster, H., Gabel, B., Nabors, B. & Cobbs, C. Glioblastoma mimicking viral encephalitis responds to acyclovir: A case series and literature review. *Front Oncol***9**, (2019).
3. Lu, J. et al. Brain astrocytoma misdiagnosed as anti-NMDAR encephalitis: a case report. *BMC Neurol***19**, (2019).
4. Panagopoulos, D., Themistocleous, M., Apostolopoulou, K. & Sfakianos, G. Herpes Simplex Encephalitis Initially Erroneously Diagnosed as Glioma of the Cerebellum: Case Report and Literature Review. *World Neurosurg.***129**, 421–427 (2019).
5. Vogrig, A. et al. Glioblastoma as differential diagnosis of autoimmune encephalitis. *J. Neurol.***265**, 669–677 (2018).
6. Śledzińska-Bebyn, P., Furtak, J., Bebyn, M. & Serafin, Z. Beyond conventional imaging: Advancements in MRI for glioma malignancy prediction and molecular profiling. *Magn. Reson. Imaging*. **112**, 63–81 (2024).
7. Han, Y. et al. Distinguishing brain inflammation from grade II glioma in population without contrast enhancement: a radiomics analysis based on conventional MRI. *Eur. J. Radiol.***134**, 109467 (2021).
8. Mayerhoefer, M. E. et al. Introduction to Radiomics. *J. Nucl. Med.***61**, 488–495 (2020).
9. Zhu, F. Y. et al. Using machine learning-based radiomics to differentiate between glioma and solitary brain metastasis from lung cancer and its subtypes. *Discover Oncol.***14**, 1–10 (2023).
10. Li, Y. et al. Radiomics-based method for predicting the glioma subtype as defined by tumor grade, IDH mutation, and 1p/19q codeletion. *Cancers 2022*. **14**, 1778 (2022).
11. Tian, Q. et al. Radiomics strategy for glioma grading using texture features from multiparametric MRI. *J. Magn. Reson. Imaging*. **48**, 1518–1528 (2018).
12. Soleymani, Y., Sheikhzadeh, P., Mohammadzadeh, M. & Khezerloo, D. Simplifying radiomics workflow for predicting grade of glioma: An approach for rapid and reproducible radiomics. *J. Biomed. Phys. Eng.***15**, 27–36 (2025).
13. Christodoulou, R. C. et al. Artificial Intelligence in Glioma Diagnosis: A Narrative Review of Radiomics and Deep Learning for Tumor Classification and Molecular Profiling Across Positron Emission Tomography and Magnetic Resonance Imaging. *Eng. 2025*. **6, Page 262** (6), 262 (2025).
14. Staal, S. L., Olie, S. E., van de Beek, D. & Brouwer, M. C. Validation of the encephalitis criteria in adults with a suspected central nervous system infection: An updated score. *J. Infect.***89**, (2024).
15. Graus, F. et al. A clinical approach to diagnosis of autoimmune encephalitis. *Lancet Neurol.***15**, 391–404 (2016).
16. Venkatesan, A. et al. Case definitions, diagnostic algorithms, and priorities in encephalitis: consensus statement of the international encephalitis consortium. *Clin. Infect. Dis.***57**, 1114–1128 (2013).

17. R Core Team. R: A language and environment for statistical computing. https://www.r-project.org/ (2025).
18. Christodoulou, R. C., Vamvouras, G., Pitsillos, R., Solomou, E. E. & Georgiou, M. F. Explainable radiomics with probability calibration for postoperative glioblastoma surveillance. *Eur. J. Radiol. Artif. Intell.***5**, 100074 (2026).
19. Chen, X. et al. Differentiation of true-progression from pseudoprogression in glioblastoma treated with radiation therapy and concomitant temozolomide by GLCM texture analysis of conventional MRI. *Clin. Imaging*. **39**, 775–780 (2015).
20. Nakagawa, M. et al. Machine learning based on multi-parametric magnetic resonance imaging to differentiate glioblastoma multiforme from primary cerebral nervous system lymphoma. *Eur. J. Radiol.***108**, 147–154 (2018).
21. Alcaide-Leon, P. et al. Differentiation of Enhancing Glioma and Primary Central Nervous System Lymphoma by Texture-Based Machine Learning. *AJNR Am. J. Neuroradiol.***38**, 1145–1150 (2017).
22. Suh, H. B. et al. Primary central nervous system lymphoma and atypical glioblastoma: Differentiation using radiomics approach. *Eur. Radiol.***28**, 3832–3839 (2018).
23. Deepak, S. & Ameer, P. M. Brain tumor classification using deep CNN features via transfer learning. *Comput Biol. Med***111**, (2019).
24. Talo, M., Yildirim, O., Baloglu, U. B., Aydin, G. & Acharya, U. R. Convolutional neural networks for multi-class brain disease detection using MRI images. *Comput. Med. Imaging Graph.***78**, (2019).
25. Yun, J. et al. Radiomic features and multilayer perceptron network classifier: a robust MRI classification strategy for distinguishing glioblastoma from primary central nervous system lymphoma. *Sci Rep***9**, (2019).
26. Yang, Y. et al. Glioma grading on conventional MR images: A deep learning study with transfer learning. *Front Neurosci***12**, (2018).
27. Zheng, F. et al. MRI-based machine learning fusion models to distinguish encephalitis and gliomas. *J. Imaging Inf. Med.* **37**, 653–665 (2024).
28. Piao, S. et al. An MRI-based joint model of radiomics and spatial distribution differentiates autoimmune encephalitis from low-grade diffuse astrocytoma. *Front. Neurol.***13**, 998279 (2022).
29. Tan, R., Sui, C., Wang, C. & Zhu, T. MRI-based intratumoral and peritumoral radiomics for preoperative prediction of glioma grade: a multicenter study. *Front. Oncol.***14**, 1401977 (2024).
30. Fan, H. et al. Artificial intelligence-based MRI radiomics and radiogenomics in glioma. *Cancer Imaging* **24**, 36 (2024).
31. Ge, C., Gu, I. Y. H., Jakola, A. S. & Yang, J. Deep learning and multi-sensor fusion for glioma classification using multistream 2D convolutional networks. *Annu. Int. Conf. IEEE Eng. Med. Biol. Soc.* 5894–5897 (2018).
32. Liang, S. et al. Multimodal 3D DenseNet for IDH Genotype Prediction in Gliomas. *Genes (Basel)***9**, (2018).
33. Sümer-Arpak, E. et al. Radiomics-based models to predict IDH mutation status and prognosis in gliomas using MRI: a multicenter study. *Front. Oncol.***16**, 1775958 (2026).

Publisher's note Springer Nature remains neutral with regard to jurisdictional claims in published maps and institutional affiliations.

Authors and Affiliations

Eliseo Picchi[1] · Carlo Di Donna[1] · Armando Ugo Cavallo[2] · Silvia Minosse[3] · Alessandro Castelli[4] · Chiara Giuseppina Bonomi[5] · Francesca Izzi[4] · Alessia Amatruda[1] · Valerio Da Ros[1] · Francesco Garaci[1,6] · Francesca Di Giuliano[6]

✉ Eliseo Picchi
eliseo.picchi@uniroma2.eu

[1] Diagnostic Imaging Unit, Department of Biomedicine and Prevention, University of Rome Tor Vergata, Via Montpellier 1, 00133 Rome, Italy

[2] Division of Radiology, Istituto Dermopatico dell' Immacolata IRCCS, Rome, Italy

[3] Diagnostic Imaging Unit, University Hospital of Rome Tor Vergata, Via Oxford 81, 00133 Rome, Italy

[4] Epilepsy Centre, Neurology Unit, Policlinico Tor Vergata, University of Rome Tor Vergata, Viale Oxford 81, 00133 Rome, Italy

[5] Memory Clinic and Neurodegenerative Dementia Research Unit, Policlinico Tor Vergata, University of Rome Tor Vergata, Viale Oxford 81, 00133 Rome, Italy

[6] Neuroradiology Unit, Department of Biomedicine and Prevention, University of Rome Tor Vergata, Via Montpellier 1, 00133 Rome, Italy